

ORIGINAL RESEARCH PAPER

## Solar Driven Photocatalysis using $\text{CoFe}_2\text{O}_4$ -CNT Nanocomposites for Degradation of hazardous Rose Bengal dye

Vikas Vikas<sup>1</sup>, Pawan S. Rana<sup>1\*</sup>

<sup>1</sup>Department of Physics, Deenbandhu Chhotu Ram University of Science & Technology, Murthal, Sonapat 131039, Haryana, India

Received: 2023-01-01

Accepted: 2023-03-28

Published: 2023-05-16

### ABSTRACT

The study involved the preparation of  $\text{CoFe}_2\text{O}_4$ -CNT nanocomposites through the dispersion of CNT and ferrites into Xylene. Cobalt ferrites were synthesized using a chemical co-precipitation method. The main objective was to investigate the structural, optical, and photocatalytic properties of the synthesized nanocomposites using Rose Bengal dye as a model pollutant. Structural analysis was conducted using Transmission Electron Microscopy (TEM) and XRD, confirming the formation of a Single-phase spinal structure of ferrites and nanocomposites with an average particle size of around 25 nm. UV-Vis. spectroscopy and Photoluminescence (PL) were used to study the optical properties of the samples, indicating that the bandgap of the sample is within the visible range, making it suitable for visible light photocatalysis. The band gap shifted to a slightly lower side after the formation of the nanocomposite, and the PL revealed that recombination time increased after the formation of nanocomposites compared to pure  $\text{CoFe}_2\text{O}_4$ . FTIR spectroscopy confirmed the formation of the spinal structure of ferrites and identified various bonds present in the sample. The photocatalytic activity of the sample showed a significant increase in the dye degradation capacity of ferrites. This increase in photocatalytic activity was consistent with earlier results obtained by PL spectroscopy, which confirmed the formation of a Z-scheme visible light photocatalyst.

**Keywords:** CNT, Nanocomposites, Z-Scheme photocatalyst, Solar energy

### How to cite this article

Vikas V., Rana P. S., Solar Driven photocatalysis using  $\text{CoFe}_2\text{O}_4$ -CNT nanocomposites for degradation of hazardous Rose Bengal dye. J. Water Environ. Nanotechnol., 2023; 8(2): 164-177 DOI: 10.22090/jwent.2023.02.006

### INTRODUCTION

Both developing and developed worlds are concerned about water pollution caused by industrial, domestic, agricultural, and commercial activities. Around 2.2 million people die due to bad-quality water every year. Around 1 billion people consume unhealthy water every day [1]. In four highly populous developing countries named China, India, Indonesia, and Brazil, aquatic life is under threat as dissolved oxygen levels are very low [2]. Being one of the most necessary gifts of nature, poor quality of water harm all kind of life. One of the major contributors to water pollution is

the textile industry. This industry is very important for the economic growth of a country. The biggest exporter of all kinds of textiles is China followed by E.U., India and then U.S.A [3]. The textile industry generates around one trillion dollars annually and contributes to 7% of the world's total export. This industry engages around 35 million workers around the globe [4]. Dyeing is an important step in this industry. Once the final product is ready, these dyes and chemicals are discharged and become part of textile effluent [5], [6]. These dyes which are used to give various magnificent colors to textiles are very harmful to both human beings and nature. Dyes are highly soluble in water so removing them

\* Corresponding Authors Email: [drpawansrana.phy@dcrustm.org](mailto:drpawansrana.phy@dcrustm.org)



This work is licensed under the Creative Commons Attribution 4.0 International License.

To view a copy of this license, visit <http://creativecommons.org/licenses/by/4.0/>.

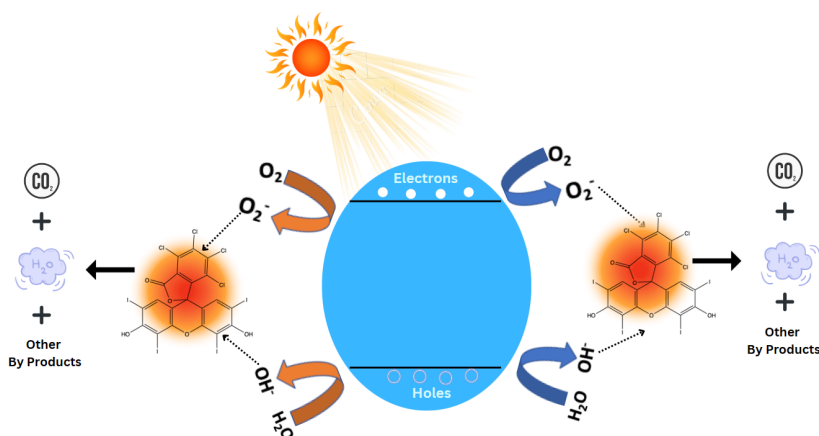


Fig. 1: Mechanism of Photocatalysis

using conventional methods is very difficult [7]. This color linked to dyes not only imparts aesthetic damage to water bodies but also reduces the rate of photosynthesis by preventing sunlight to penetrate water hence reducing in dissolved oxygen rate thereby harming entire aquatic life as all forms of aquatic life are closely related to each other [8].

Scientists are constantly working to find a reliable solution to treat industrial wastewater [9]–[19]. The advanced Oxidation Process (AOP) seems to be a promising way to remove these harmful contaminants from water. This process relies on highly reactive hydroxyl ions ( $\bullet\text{OH}$ ) to oxidize the organic (sometimes inorganic) pollutants from water which cannot be removed by traditional techniques [20]–[23]. Using the light wave of suitable frequency to perform AOP is called photocatalysis. Much Attention is being paid recently to developing photocatalysts to treat wastewater and for hydrogen generation [24]–[26]. Water purification is one of the most useful applications of photocatalysis. Photocatalysis happens by utilizing an electromagnetic wave of suitable energy to produce electron-hole pairs in the semiconductor. Electrons and holes help to produce superoxide and hydroxyl radicals which attack on dye to degrade it into water,  $\text{CO}_2$  and other less harmful byproducts as shown in Fig. 1. Metal oxides seemed to be promising photocatalyst but it suffers from two major drawbacks. Recovery of metal oxide after treatment of wastewater is not very easy and hence, it can't be employed for large-scale water purification. The band gap of metal oxides lies in UV and most of the UV radiation from the sun is blocked by the ozone layer so they

don't reach the earth's surface we have to depend on UV lamp to make it work as photocatalyst and hence power consumption is also a major drawback of this photocatalyst [27], [28]. Ferrites fulfill the above two conditions as they are paramagnetic so they can be separated after treatment of wastewater just by using strong magnets [29]. The band gap of ferrites also lies in the visible so it can harness sunlight to act as a photocatalyst without any external power source other than the sun [13], [22], [30]. This low value of band gap has one drawback and that is a higher rate of recombination of electrons and holes. Hence electrons and holes are available only for a very short period to perform photocatalysis and hence the rate of degradation of dye is very less [31], [32]. The above problem is solved by making a Z-Scheme heterojunction photocatalyst by anchoring ferrite nanoparticles on the CNT matrix. It provides an alternative path for electrons to return to the valence band and hence it increases the value of recombination time [33], [34]. CNTs have a very high value of surface area so it also helps in the adsorption of dyes on their surface hence we get the better photocatalytic activity of synthesized nanocomposites. Ferrites get attracted to magnets so nanoparticles can be easily removed by applying an external magnetic field and can be used again. Hence the problem of recovery of the sample is eliminated by a significant amount.

In this present study, we studied the effect of the formation of a z-scheme photocatalyst on the photocatalytic performance of  $\text{CoFe}_2\text{O}_4$  for the removal of harmful Rose Bengal dye. To our knowledge, it has not been reported

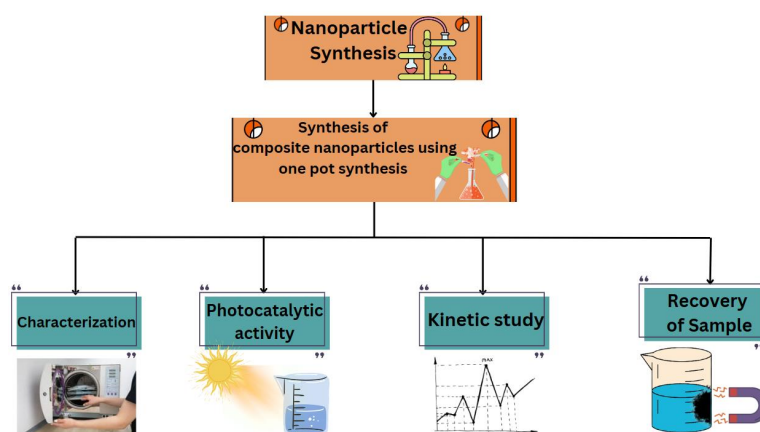


Fig. 2: Graphical research overview of work

yet about the photocatalytic application of Co Ferrite nanocomposite with CNT. Various factors responsible for this change in photocatalytic activity are studied with the help of XRD, TEM, FT-IR, UV-Vis, Photoluminescence, and VSM. The z-scheme mechanism is proposed to explain why photogenerated electron-hole pairs have longer recombination times. The photocatalytic activity was studied in the presence of sunlight with continuous stirring using a non-magnetic stirrer. Recovery of the sample was studied by using the same photocatalyst again for three consecutive cycles. The research methodology for this work is shown in Fig. 2.

## EXPERIMENTAL

### Materials

Following precursors were used for the preparation of  $\text{CoFe}_2\text{O}_4$  and its nanocomposites with CNT:  $\text{Fe}(\text{NO}_3)_3 \cdot 3\text{H}_2\text{O}$  manufactured by Sigma Aldrich having purity >98%,  $\text{Co}(\text{NO}_3)_2 \cdot 6\text{H}_2\text{O}$  from SRL Chemicals having purity > 98%, Multi-Walled Carbon Nano Tubes (MWCNT) having -COOH Functional group attached to them with outer diameter 30-50 nm and length 10-30  $\mu\text{M}$  Manufactured by SRL Chemicals, Xylene is used from fisher scientific.

### Synthesis of cobalt ferrite (CoF)

Cobalt Ferrite nanoparticles were synthesized by the chemical co-precipitation method. Aqueous solutions of  $\text{Fe}(\text{NO}_3)_3 \cdot 3\text{H}_2\text{O}$  and  $\text{Co}(\text{NO}_3)_2 \cdot 6\text{H}_2\text{O}$  were mixed in different beakers according to the stoichiometric ratio. Both solutions were placed on a magnetic stirrer and stirred individually at  $50^\circ\text{C}$

for 15 minutes. Both solutions were then mixed and stirring was continued for 30 minutes. 10 ml of oleic acid was then added to prevent agglomeration. The sample was further heated for 30 more minutes at the same temperature. The magnetic bead was then removed to prevent the sticking of ferrites to the magnetic bead. Ammonia was then used as a precipitating agent and added dropwise to the sample along with manual stirring. pH was monitored closely as ammonia is being added to the sample. We will notice that precipitates will start forming. Ammonia addition is stopped once the pH level reaches 10. The sample was then dried at  $80^\circ\text{C}$  for 2 hours to remove residual water present in the sample. The sample was then washed several times with distilled water to remove any dissolved impurities. The sample was then further dried at  $80^\circ\text{C}$  for two hours and then crushed finely using a mortar and pestle. Annealing was done at  $400^\circ\text{C}$  for proper phase growth.

### Fabrication of cobalt ferrite-CNT nanocomposites (CoF-CNT)

MWCNT functionalized with -COOH group were dispersed in Xylene by sonication for 30 minutes. Ferrites were also dispersed in Xylene in another beaker by sonication for 30 minutes. Ferrite dispersion was then added dropwise into CNT dispersion. The obtained dispersion was then left to dry in a hot air oven at  $80^\circ\text{C}$  for 12 hours. The obtained powder was then crushed and annealed at  $400^\circ\text{C}$  for 2 hours in a tubular furnace.

### Characterization of sample

Following characterization methods were used

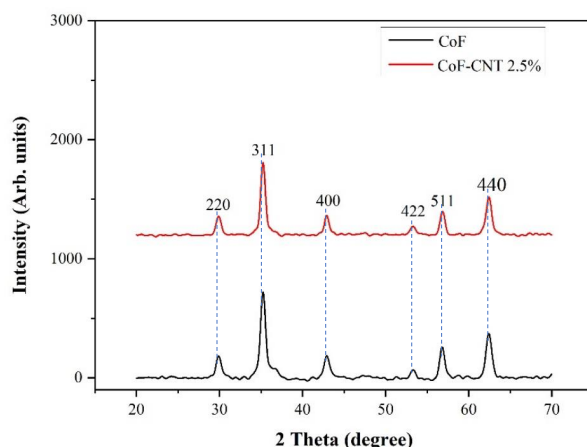


Fig. 3: XRD data of CoF and CoF-CNT

to study various properties of nanoparticles:

#### X-Ray Diffraction (XRD)

X-ray diffraction (XRD) was performed on the samples using a Rigaku Ultima IV diffractometer ( $\lambda = 1.54 \text{ \AA}$  of Cu- $\alpha$  radiation) at room temperature with a copper anti-cathode operated at 40 kV and 40 mA. The purpose of this analysis was to identify whether the structure of the samples was crystalline or amorphous. The powder samples were evenly distributed on a neutral quartz glass sample holder and exposed to a k-alpha radiation source. The diffraction scans were conducted over a range of angles from  $10^\circ$  to  $80^\circ$ . The average crystallite size was calculated by using Debye-Scherrer's formula

$$D = \frac{k\lambda}{\beta \cos\theta_{311}} \quad (1)$$

where  $\lambda = 1.5406$  is the wavelength of CuK $\alpha$  radiations,  $k=0.9$  is the shape factor, and  $\theta_{311}$  and  $\beta$  are Bragg's angle and FWHM respectively corresponding to the plane (311) [35].

#### Fourier Transform Infrared Spectroscopy (FTIR)

Material analysts utilize FTIR to identify the Various bonds present in a given sample. To obtain the FTIR spectra of a sample, we used Perkin Elmer FTIR Spectrum 2 instrument and record the data within the  $4000\text{cm}^{-1}$  to  $400 \text{ cm}^{-1}$  wavenumber range. The FTIR spectra are obtained by combining the sample with KBr powder at a 5:95 ratio to create KBr pellets using a hydraulic press-assisted pelletizer.

#### UV-Vis analysis

Analysis of optical absorption spectra is a very

efficient tool for understanding the band structure and energy gap of spinal structure materials [36]. UV-Vis analysis was done using Shimadzu UV 3600 I PLUS UV-Vis spectrometer. The band gap is calculated using a tauc plot. The general equation of the Tauc plot method is given by,

$$(\alpha h\nu)^n = K(h\nu - E_g) \quad (3)$$

Here ' $h\nu$ ' is the incident photon energy, ' $\alpha$ ' is the absorption coefficient, ' $E_g$ ' is the bandgap energy, ' $K$ ' is an energy-independent constant, and ' $n$ ' is the nature of the transition. Any one of the following four values can describe the nature of the transition,  $n$  [37],

- $n = 2$  - direct allowed transition
- $n=1/2$ - Indirect allowed transition
- $n=2/3$ - Forbidden Direct Transition
- $n=1/3$ - Forbidden Indirect Transition

#### Photoluminescence (PL)

Photoluminescence (PL) spectra were obtained using a Horiba Scientific Fluoromax+ spectrofluorometer. PL is a widely used tool to study the efficiency of charge carrier trapping and to understand the fate of charge carriers and their recombination in semiconductors [38], [39]. PL gives all information by studying the emission of light from a material after it has been excited by an external energy source. When a material is excited, its electrons are promoted to higher energy states. As the electrons relax back to their ground state, they emit energy in the form of light. The emitted light can be measured and analyzed to obtain information about the electronic and optical properties of the material.

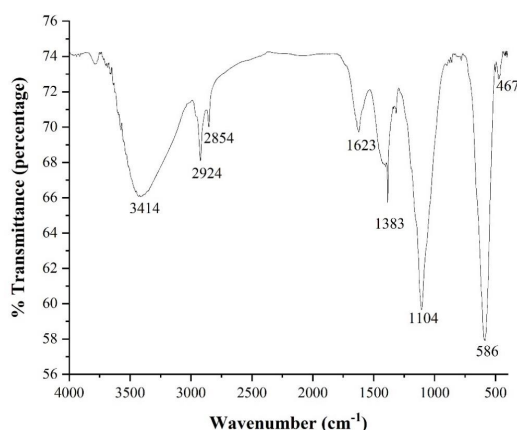


Fig. 4: FTIR Spectra of CoF

### Transmission Electron Microscopy (TEM)

TEM is a powerful analytical technique that allows for high-resolution imaging of the internal structure and composition of materials. It works by passing a beam of electrons through a thin sample, which interacts with the nanoparticles to produce an image. When the electron beam passes through the sample, it interacts with the atoms within the material. This interaction scatters the electrons and produces a pattern of bright and dark areas, which can be captured by the detector and used to generate an image. Transmission Electron Microscopy (TEM) images were obtained using JEOL JEM-1400 plus having 120 kV accelerating voltage.

### Vibrating Sample Magnetometry (VSM)

Vibrating Sample Magnetometry (VSM) is a commonly used experimental technique to measure the magnetic properties of materials. In VSM analysis, a sample is placed in a magnetic field and subjected to a small oscillating magnetic field perpendicular to the applied field. The resulting changes in the magnetic moment of the sample are measured using a highly sensitive detector, such as a Hall sensor or a magnetometer. VSM data was obtained using CFMS from cryogenic limited, UK at IIT Delhi Sonipat Campus at room temperature.

## RESULTS AND DISCUSSION

### X-Ray diffraction (XRD) analysis

Fig. 3 shows the XRD pattern of  $\text{CoFe}_2\text{O}_4$  and their nanocomposites with CNT. Indexing of diffraction peaks was done at various  $2\theta$  values and all Characteristic peaks which belong to planes (220), (311), (400), (422), (511), and (440) can be

indexed in the single-phase lattice. The position and relative intensity of all peaks correspond well with standard data of Cobalt ferrite powder diffraction data (JCPDS card no. 22-1086). Various peaks are labeled in the graph. No diffraction peak for any other phase or any other material is observed which indicates that there was no secondary phase or any impurity precipitates in the sample. The most intense peak (311) was used to find crystallite size (D). we found that the average crystallite size for CoF is 20.14 nm. Lattice parameter (a) was calculated using the interplanar spacing  $d$  (Å)

$$a = d\sqrt{h^2 + k^2 + l^2} \quad (2)$$

a is found to be 8.402 Å

### FTIR Spectroscopy

FTIR analysis was done with Perkin-Elmer Frontier. KBr pellets were used and data was recorded in the Wavenumber range 400-4000  $\text{cm}^{-1}$  and is shown in Fig. 4. FTIR spectra show various functional groups attached as shown in Table 1 below and indicated on the graph. The peak at 467  $\text{cm}^{-1}$ ,  $\nu_2$ , shows intrinsic metal-oxygen bond stretching vibrations at octahedral sites, and that at 586  $\text{cm}^{-1}$ ,  $\nu_1$ , shows intrinsic Metal-oxygen bond stretching vibrations at tetrahedral sites. These peaks are the main metal-oxygen bond peaks that are seen for all spinal ferrites so they confirm the formation of the spinal structure of ferrites [40]. The peak at 1104  $\text{cm}^{-1}$  is because of the C-O-C bond. At 1383  $\text{cm}^{-1}$ , the peak is due to the nitrate group present as residue. The peak at 1623  $\text{cm}^{-1}$  and 3414  $\text{cm}^{-1}$  is because of water absorbed by KBr. The peak at 2854 and 2924 corresponds to

Table 1. Various bonds present in the sample as confirmed by FTIR Spectroscopy

Wavenumber ( $\text{Cm}^{-1}$ )	Bond
467	Metal-Oxygen bonds at Octahedral sites
586	Metal-Oxygen bonds at Tetrahedral sites
1104	C-O-C
1383	Nitrate group present as residue
1623	H-O-H
2854	C-H
2924	C-H
3414	H-O-H

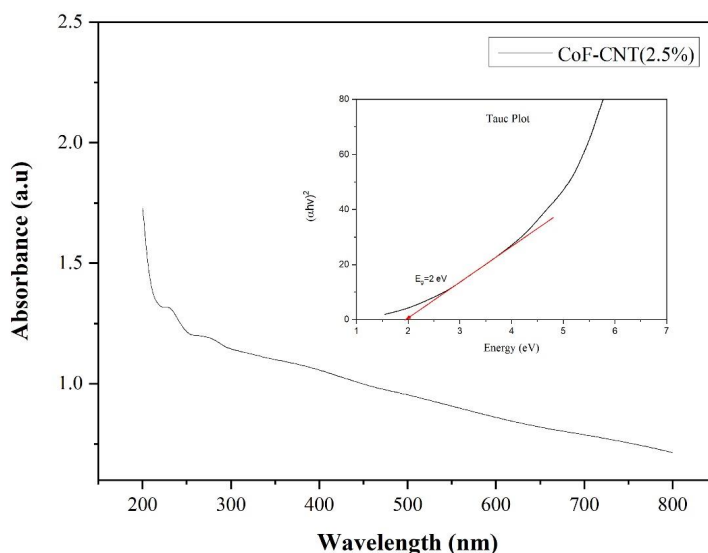


Fig. 5: UV-Vis Spectra of CoF-CNT with Tauc Plot

symmetric and anti-symmetric bond stretching of the C-H bond [41].

#### UV-Vis Analysis

UV-Vis spectroscopy output is shown in Fig. 5 for CoF and CoF-CNT respectively. The optical absorption data shows that in the case of both CoF and CoF-CNT, we do not get any steep edges or shoulder-like structures, indicating that visible light absorption is due to intrinsic band transition and may not be due to surface states [42]. For a normal spinel-type material (CoF), Octahedral and tetrahedral sites are occupied by  $\text{Fe}^{3+}$  and  $\text{Co}^{2+}$

respectively [43]. In general, the band structure of CoF was explained by using the oxygen 2p orbital as the valance band and the Fe 3d orbital as the conduction band [44]. The absorption in the area of visible light may be caused by electron excitation from the 2p orbital of oxygen to the 3d level of Fe. In the case of CoF-CNT, we get some intermediate state between this energy gap which provides an alternative path for electrons to recombine, and hence band gap gets reduced slightly. UV-Vis spectra show that the band gap of synthesized nanoparticles lies in the visible light region of the electromagnetic spectrum.  $(\alpha h\nu)^n$  was plotted as a

Table 2. Various magnetic parameters of the sample

Sample Name	Saturation Magnetization (M <sub>s</sub> )	Retentivity (M <sub>r</sub> )	Coercivity (H <sub>c</sub> )
CoF	88.08	33.18	-1350
CoF-CNT	44.69	19.38	-1507

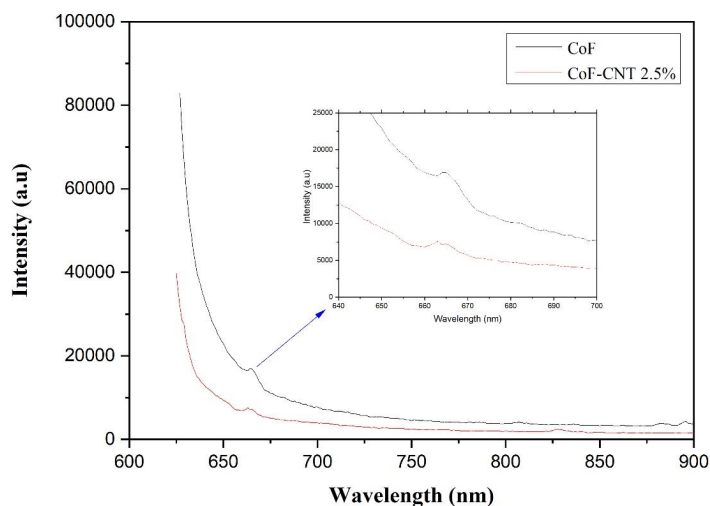


Fig. 6: PL spectra of CoF and CoF-CNT

function of the photon energy  $h\nu$  for different  $n$  and we found that the best linear fit was obtained for  $n=2$  so we came to know that it is a direct allowed band gap. The linear part was extrapolated to the point where it intersects the x-axis and that point gives the value of the band gap of the material as shown in the inset images of the graph. The band gap of CoF is 2.15 eV and is 2 eV for CoF-CNT. The band gap is slightly decreasing after the formation of nanocomposites. This value of bandgap confirms that our sample can be used for solar-driven photocatalytic application.

#### Photoluminescence

Fig. 6 shows the photoluminescence spectra of CoF and CoF-CNT. PL spectra show that the sample emits at around 664 nm when excited at a suitable frequency. Peak intensity is found to decrease in the case of nanocomposites. This decrease in the peak of PL spectra for nanocomposites is in good agreement with the theory. The decrease in peak intensity shows that the rate of radiative transition has decreased due to the trapping of charge carriers, this confirms that the formation of nanocomposites hinders the recombination rate

and hence it improves photocatalytic activity [39], [45]. This is in good agreement with experimental data obtained from photocatalysis experiments. Hence it is confirmed that CoF-CNT 2.5% forms a better visible light photocatalyst.

#### Transmission Electron Microscopy

Fig. 7 shows TEM images of CoF and CoF-CNT. Carbon Nanotubes (CNT) can be seen clearly in TEM images. CoF nanoparticles can also be seen clearly in images and it is also observed that CoF is anchored to CNT at various points. This confirms the formation of nanocomposites. Fig. 8 shows the size distribution chart for CoF nanoparticles. It was found that the average size of CoF nanoparticles is around 25 nm.

#### Vibrating Sample Magnetometry (VSM) Analysis

The room temperature magnetic hysteresis loop has been shown in Fig. 9 which indicates ferrimagnetic behavior marked by the appearance of the hysteresis loop i.e., non-zero values of coercivity and retentivity. Various magnetic parameters corresponding to the plots are listed in Table 2. It has been found that the value of Saturation Magnetization ( $M_s$ ) and

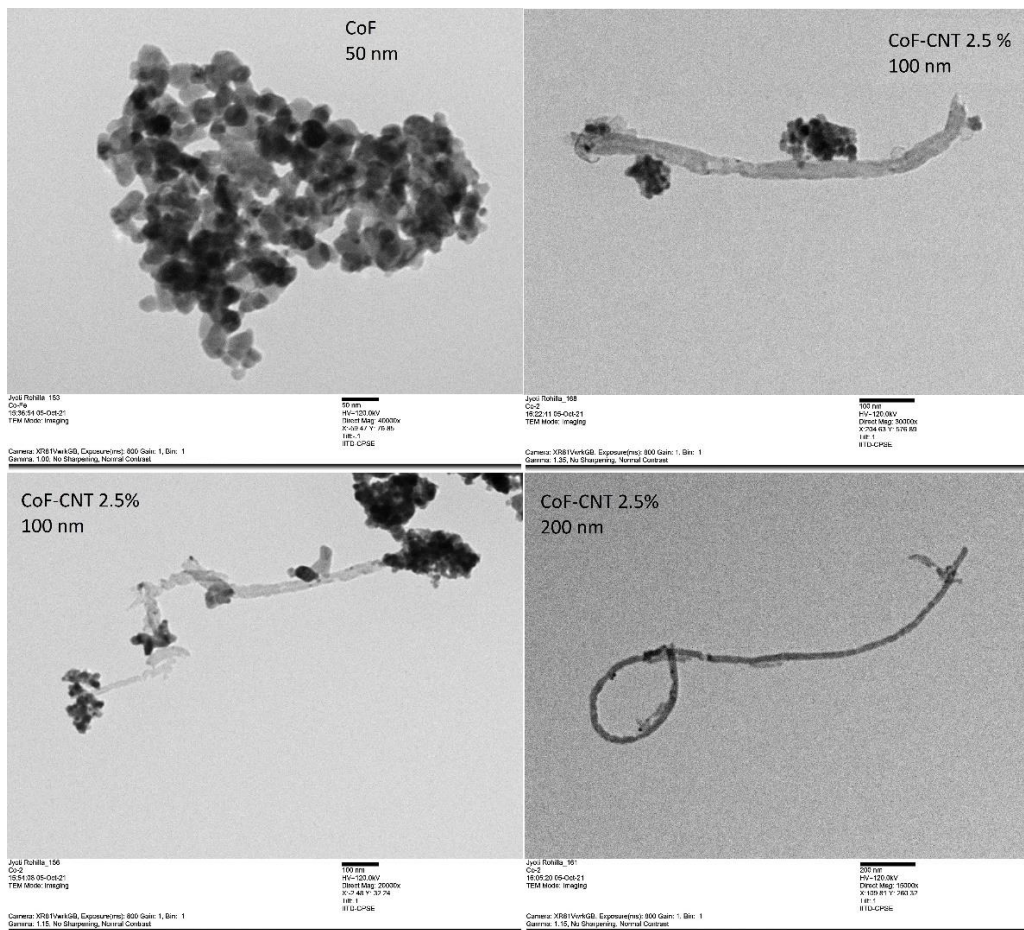


Fig. 7: TEM images of CoF and CoF-CNT at various scales

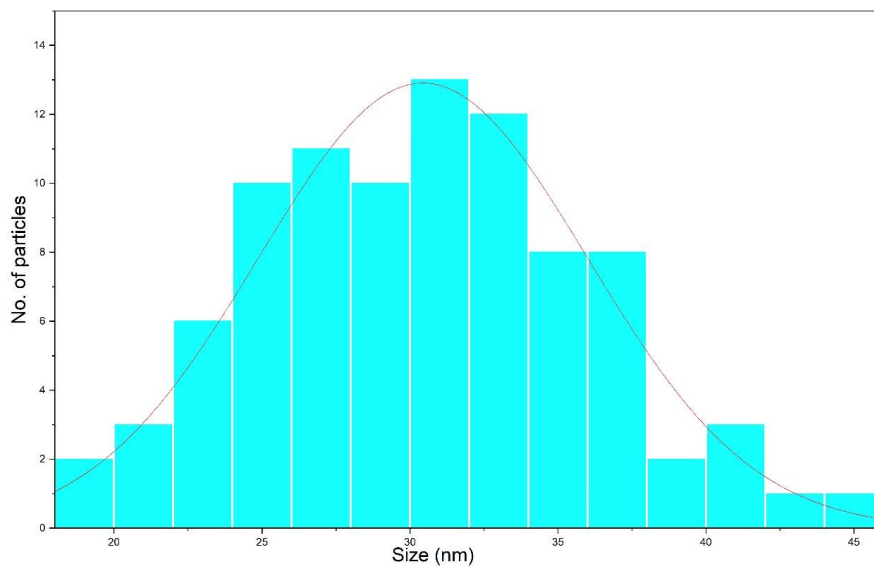


Fig. 8: Size distribution of nanoparticles as observed by TEM

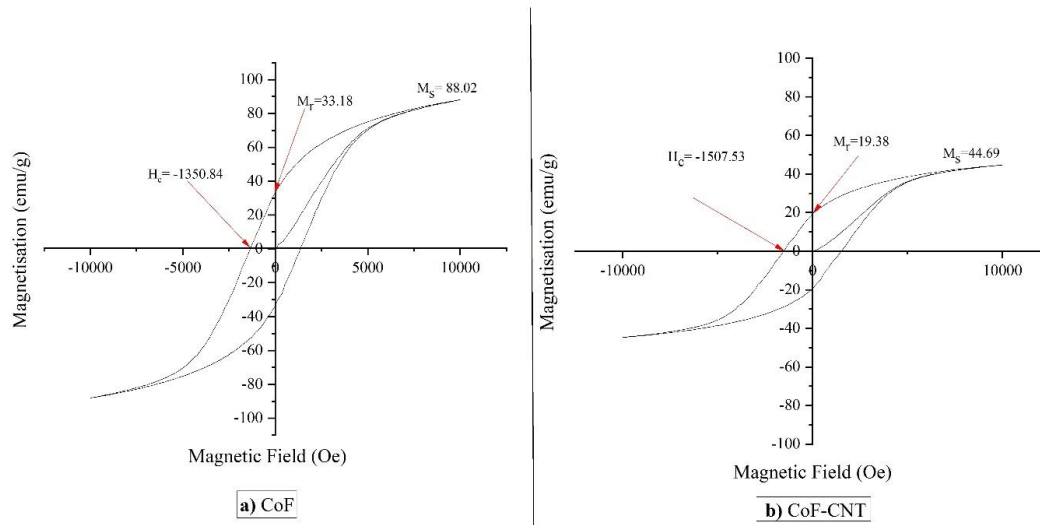


Fig. 9: VSM Data for a) CoF and b) CoF-CNT

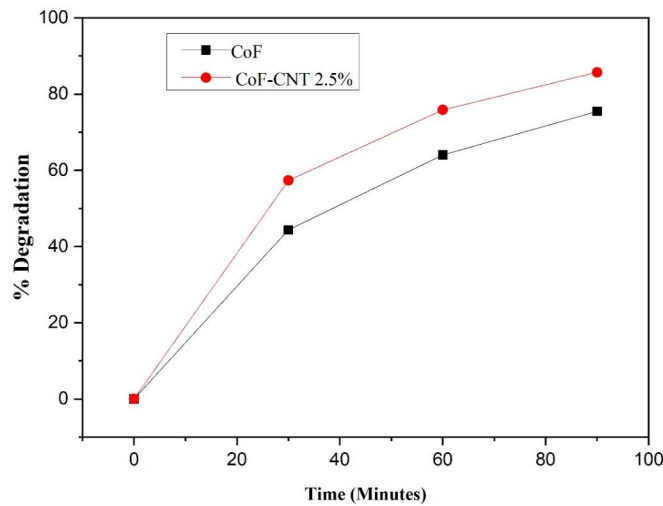


Fig. 10: Photocatalysis data of CoF and CoF-CNT

remanent magnetization ( $M_r$ ) has decreased after the formation of nanocomposites. This can be attributed to the presence of non-magnetic CNTs and structural deformation in the structure of the ferrite. Although pure CNTs are not magnetic by nature, when a magnetic field is present, the non-magnetic particles act as voids and disrupt the magnetic circuits, which causes magnetization to decline [46]. Structural deformation occurs because of the interaction between oxygen and the transition metal (in this case, cobalt) in the cubic lattice, which lowers the magnetic moment of the nanoparticles [46], [47].

#### Photocatalytic activity

Photocatalysis was performed by direct irradiation under sunlight at DCRUST Murthal having latitude  $29.0272^\circ$  N and longitude  $77.0621^\circ$  E. Sunlight intensity was measured using a flux meter and found to average around 93000 Lux. The band gap of synthesized nanoparticles lies well in the visible light range of the Electromagnetic Spectrum so natural sunlight was used for photocatalysis. 50 mg of CoF was mixed in 100 ml of 10 ppm Rose Bengal dye (5g/L) and stirred using a mechanical stirrer in the dark for 30 minutes to achieve adsorption-desorption equilibrium. Then the

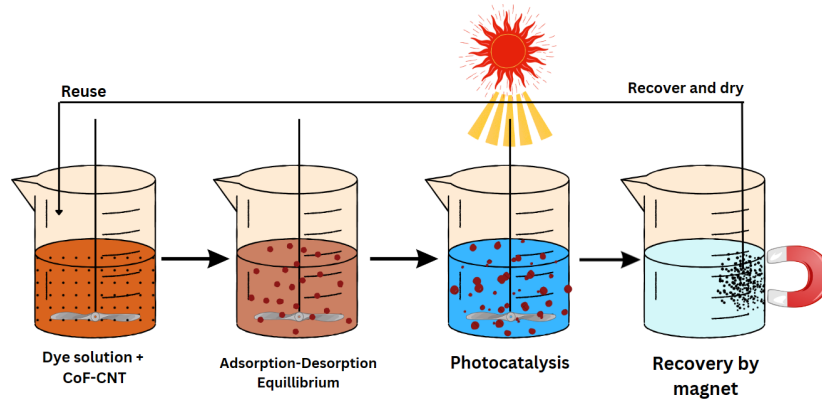


Fig. 11: Photocatalysis and recovery of sample

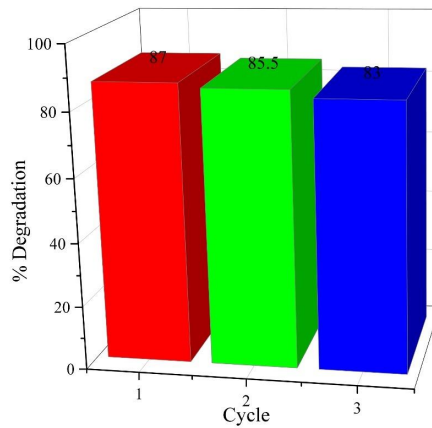


Fig. 12: Reusability of sample

sample was placed under direct sunlight and stirring was continued. 5 ml sample was taken at regular intervals to find the amount of degradation with time. This sample is then placed under the magnetic influence to remove the photocatalyst present in them. UV was then done immediately to get the exact percentage of degradation of the dye. The same process was repeated for CoF-CNT and it was found that CoF-CNT is more effective in the photocatalytic degradation of dye as shown in Fig. 10. Percentage degradation was calculated using the formula

$$\% \text{Degradation} = \left(1 - \frac{C}{C_0}\right) \times 100 \quad (4)$$

Where  $C_0$  is the initial concentration and  $C$  is the concentration at that instant of time. It was found that 87% of dye was degraded in 90 minutes of irradiation by CoF-CNT nanocomposites which

is better than CoF nanoparticles which degrade around 73% of dye at the same time. This higher efficiency is attributed to the longer recombination time of electrons and holes in photocatalysts [48]. A comparison table is shown below to show the efficiency of various photocatalysts based on ferrite nanoparticles. Kinetics data was obtained by using a graph of  $\ln(C_0/C)$  according to Langmuir- The hinshelwood kinetic model. The rate of reaction can be obtained as:

$$r = \frac{dC}{dt} = \frac{kKC}{1+KC} \quad (5)$$

The variables in the equation are  $r$ , which represents the rate of the reactant in milligrams per liter per minute;  $C$ , the concentration of the reactant in milligrams per liter;  $t$ , the illumination time;  $k$ , the rate constant of the reaction in milligrams per liter per minute; and  $K$ , the adsorption coefficient

Table 3. Summary of recently used ferrite nanocomposites in wastewater treatment and their corresponding efficiency

Type of ferrite nanoparticle	Pollutant	Contact Time (min)	Catalyst dose (g l <sup>-1</sup> )	Pollutant Concentration (mg l <sup>-1</sup> )	Light source	Removal Capacity	Ref.
Ag/TiO <sub>2</sub> /NiFe <sub>2</sub> O <sub>4</sub>	Methyl Orange	120	1	10	Visible light	90%	[50]
Fe <sub>3</sub> O <sub>4</sub> /TiO <sub>2</sub>	Methylene Blue	240	0.2	10	UV Light	50%	[51]
ZnFe <sub>2</sub> O <sub>4</sub> /TiO <sub>2</sub>	RhB	90	0.45	4.8	UV Light	81%	[52]
MgFe <sub>2</sub> O <sub>4</sub>	Methylene Blue	240	0.2	10	Visible Light	85%	[53]
MoS <sub>2</sub> /CoFe <sub>2</sub> O <sub>4</sub>	RhB	90	0.6	5	Sunlight	78%	[54]
CoFe <sub>2</sub> O <sub>4</sub> /CNT (This work)	Rose Bengal	90	0.5	50	Sunlight	87%	-

of the reactant in liters per milligram. When the concentration of the chemical C is low, the equation can be simplified to an apparent first-order equation [49]:

$$\ln \frac{C_0}{C} = kt \quad (6)$$

The value of R-square for photocatalytic degradation of Rose Bengal dye was 0.96 and 0.99 for straight line fit using CoF and CoF-CNT respectively. This suggests that the reaction follows first-order kinetics.

#### Recovery of Sample

Recovery of the sample was studied by using the same photocatalyst for the degradation of dye for 3 consecutive cycles. Each cycle is of 90 minutes. The photocatalyst was first mixed with 100 ml of 10ppm dye solution and stirred under the dark for 15 minutes to achieve adsorption-desorption equilibrium. The sample was then exposed to light and stirring was continued. After 90 minutes, a strong neodymium magnet was placed under the beaker and the sample was allowed to settle for 5 minutes. Then a reading was taken from that solution and the remaining solution was poured out of the beaker. 100 ml of dye solution was again added to this beaker and the same sample was used to degrade this dye. This cycle is again repeated to get one more result. This mechanism of photocatalysis and recovery of the sample is illustrated in Fig. 11 For the first cycle, the sample was able to degrade dye up to 87% of the dye in 90 minutes. Similarly, for the second and third cycles, the sample was able to degrade at 85.5% and 83% respectively as shown

in Fig. 12. This confirms that our sample can be used as a reusable photocatalyst. The Summary of recently used ferrite nanocomposites in wastewater treatment and their corresponding efficiency is shown in Table 3.

#### CONCLUSION

CNT-Ferrite nanocomposites have been synthesized successfully as confirmed by the XRD and TEM data. TEM shows that nanocomposites have been synthesized successfully and XRD confirms the formation of the spinal structure of nanoparticles and the size of particles is around 25 nm. FTIR further confirms the formation of spinal structure as a Metal-Oxygen bond can be seen for both tetrahedral and octahedral voids. The band gap of synthesized nanoparticles lies in the visible range as confirmed by UV-Vis spectroscopy data hence sample can act as a solar active photocatalyst. Photocatalytic activity has been increased in the case of nanocomposite. This can be attributed to the formation of a Z-scheme heterojunction photocatalyst. due to the formation of z scheme heterojunction photocatalyst, the recombination of electrons and holes is hindered, and hence electrons and holes are separated for a longer period which results in better photocatalytic activity of nanocomposites. Recovery of the sample is possible because of the ferrimagnetic behavior of synthesized nanoparticles as confirmed by VSM analysis. Hence our material can act as an efficient and reusable photocatalyst under solar irradiation thereby utilizing solar energy and using it for removal of organic dyes from textile wastewater.



## ACKNOWLEDGMENT

The authors would like to acknowledge DST-FIST lab DCRUST Murthal for using characterization equipment.

## CONFLICT OF INTEREST

The authors declare no conflict of interest.

## REFERENCES

1. F. R. Rijsberman, "Water scarcity: Fact or fiction?," *Agric. Water Manag.*, vol. 80, no. 1-3, pp. 5-22, Feb. 2006, doi: 10.1016/j.agwat.2005.07.001. <https://doi.org/10.1016/j.agwat.2005.07.001>
2. S. Olmstead and J. Zheng, "Water Pollution Control in Developing Countries: Policy Instruments and Empirical Evidence," *Rev. Environ. Econ. Policy*, vol. 15, no. 2, pp. 261-280, Jun. 2021, doi: 10.1086/715645. <https://doi.org/10.1086/715645>
3. A. E. Ghaly, R. Ananthashankar, M. Alhattab, and V. vasudevan ramakrishnan, "Production, characterization and treatment of textile effluents: A critical review," *J Chem Eng Process Technol*, vol. 5, Jan. 2014. <https://doi.org/10.4172/2157-7048.1000182>
4. A. Desore and S. A. Narula, "An overview on corporate response towards sustainability issues in textile industry," *Environ. Dev. Sustain.*, vol. 20, no. 4, pp. 1439-1459, Aug. 2018, doi: 10.1007/s10668-017-9949-1. <https://doi.org/10.1007/s10668-017-9949-1>
5. Z. Carmen and S. Daniela, *Textile Organic Dyes - Characteristics, Polluting Effects and Separation/ Elimination Procedures from Industrial Effluents - A Critical Overview*. IntechOpen, 2012. doi: 10.5772/32373. <https://doi.org/10.5772/32373>
6. A. Shokri and K. Mahanpoor, "Removal of Ortho-Toluidine from Industrial Wastewater by UV/TiO<sub>2</sub> Process," *J. Chem. Health Risks*, vol. 6, no. 3, Jun. 2016, doi: 10.22034/jchr.2016.544149.
7. M. M. Hassan and C. M. Carr, "A critical review on recent advancements of the removal of reactive dyes from dyehouse effluent by ion-exchange adsorbents," *Chemosphere*, vol. 209, pp. 201-219, Oct. 2018, doi: 10.1016/j.chemosphere.2018.06.043. <https://doi.org/10.1016/j.chemosphere.2018.06.043>
8. M. Imran, D. E. Crowley, A. Khalid, S. Hussain, M. W. Mumtaz, and M. Arshad, "Microbial biotechnology for decolorization of textile wastewaters," *Rev. Environ. Sci. Biotechnol.*, vol. 14, no. 1, pp. 73-92, Mar. 2015, doi: 10.1007/s11157-014-9344-4. <https://doi.org/10.1007/s11157-014-9344-4>
9. M. Naik, H. S. B. Naik, G. Nagaraju, M. Vinuth, K. Vinu, and S. K. Rashmi, "Effect of aluminium doping on structural, optical, photocatalytic and antibacterial activity on nickel ferrite nanoparticles by sol-gel auto-combustion method," *J. Mater. Sci. Mater. Electron.*, vol. 29, no. 23, pp. 20395-20414, Dec. 2018, doi: 10.1007/s10854-018-0174-y. <https://doi.org/10.1007/s10854-018-0174-y>
10. Madhukara Naik, H. S. Bhojya Naik, G. Nagaraju, M. Vinuth, K. Vinu, and R. Viswanath, "Green synthesis of zinc doped cobalt ferrite nanoparticles: Structural, optical, photocatalytic and antibacterial studies," *Nano-Struct. Nano-Objects*, vol. 19, p. 100322, Jul. 2019, doi: 10.1016/j.nanoso.2019.100322. <https://doi.org/10.1016/j.nanoso.2019.100322>
11. A. Arimi, L. Megatif, L. I. Granone, R. Dillert, and D. W. Bahnemann, "Visible-light photocatalytic activity of zinc ferrites," *J. Photochem. Photobiol. Chem.*, vol. 366, pp. 118-126, Nov. 2018, doi: 10.1016/j.jphotochem.2018.03.014. <https://doi.org/10.1016/j.jphotochem.2018.03.014>
12. A. A. Aziz, K. S. Yong, S. Ibrahim, and S. Pichiah, "Enhanced magnetic separation and photocatalytic activity of nitrogen doped titania photocatalyst supported on strontium ferrite," *J. Hazard. Mater.*, vol. 199-200, pp. 143-150, Jan. 2012, doi: 10.1016/j.jhazmat.2011.10.069. <https://doi.org/10.1016/j.jhazmat.2011.10.069>
13. L. V. Bora and R. K. Mewada, "Visible/solar light active photocatalysts for organic effluent treatment: Fundamentals, mechanisms and parametric review," *Renew. Sustain. Energy Rev.*, vol. 76, pp. 1393-1421, Sep. 2017, doi: 10.1016/j.rser.2017.01.130. <https://doi.org/10.1016/j.rser.2017.01.130>
14. J. C. Colmenares, R. Luque, J. M. Campelo, F. Colmenares, Z. Karpiński, and A. A. Romero, "Nanostructured Photocatalysts and Their Applications in the Photocatalytic Transformation of Lignocellulosic Biomass: An Overview," *Materials*, vol. 2, no. 4, pp. 2228-2258, Dec. 2009, doi: 10.3390/ma2042228. <https://doi.org/10.3390/ma2042228>
15. G. Fan, J. Tong, and F. Li, "Visible-Light-Induced Photocatalyst Based on Cobalt-Doped Zinc Ferrite Nanocrystals," *Ind. Eng. Chem. Res.*, vol. 51, no. 42, pp. 13639-13647, Oct. 2012, doi: 10.1021/ie201933g. <https://doi.org/10.1021/ie201933g>
16. M. A. Johar, R. A. Afzal, A. A. Alazba, and U. Manzoor, "Photocatalysis and Bandgap Engineering Using ZnO Nanocomposites," *Adv. Mater. Sci. Eng.*, vol. 2015, pp. 1-22, 2015, doi: 10.1155/2015/934587. <https://doi.org/10.1155/2015/934587>
17. A. Shokri, "Application of Electrocoagulation Process for the Removal of Acid Orange 5 in Synthetic Wastewater." [https://www.ijcce.ac.ir/article\\_30593.html](https://www.ijcce.ac.ir/article_30593.html) (accessed Feb. 06, 2023).
18. A. Shokri, M. Salimi, and T. Abmatin, "Employing photo Fenton and UV/ZnO processes for removing Reactive red 195 from aqueous environment.," *Fresenius Environ. Bull.*, vol. 26, no. 2-A, pp. 1560-1565, 2017.
19. C. Kaur, T. Roy, S. Das, R. Gupta, and T. Pramanik, "Preparation and application of bio-adsorbent for the removal of water hardness: conversion of a waste to a value-added material," *Biomass Convers. Biorefinery*, pp. 1-11, 2021. <https://doi.org/10.1007/s13399-021-01806-1>
20. M. Hazarika, P. Chinnamuthu, and J. P. Borah, "MWCNT decorated MnFe<sub>2</sub>O<sub>4</sub> nanoparticles as an efficient photo-catalyst for phenol degradation," *J. Mater. Sci. Mater. Electron.*, vol. 29, no. 14, pp. 12231-12240, Jul. 2018, doi: 10.1007/s10854-018-9334-3. <https://doi.org/10.1007/s10854-018-9334-3>
21. X. Liu, T. Zhang, D. Xu, and L. Zhang, "Microwave-Assisted Catalytic Degradation of Crystal Violet with Barium Ferrite Nanomaterial," *Ind. Eng. Chem. Res.*, vol. 55, no. 46, pp. 11869-11877, Nov. 2016, doi: 10.1021/acs.iecr.6b01762. <https://doi.org/10.1021/acs.iecr.6b01762>
22. B. Ren, Y. Huang, C. Han, M. N. Nadagouda, and D. D. Dionysiou, "Ferrites as Photocatalysts for Water Splitting and Degradation of Contaminants," in *ACS Symposium Series*, vol. 1238, V. K. Sharma, R. Doong, H. Kim, R. S. Varma, and



- D. D. Dionysiou, Eds. Washington, DC: American Chemical Society, 2016, pp. 79-112. doi: 10.1021/bk-2016-1238.ch003. <https://doi.org/10.1021/bk-2016-1238.ch003>
23. A. Shokri, "Photocatalytic degradation of nitrotoluene in synthetic wastewater by  $\text{CoFe}_2\text{O}_4/\text{SiO}_2/\text{TiO}_2$  nanoparticles using Box-Behnken experimental design," *DESALINATION WATER Treat.*, vol. 247, pp. 92-99, 2022, doi: 10.5004/dwt.2022.28037. <https://doi.org/10.5004/dwt.2022.28037>
  24. J. Ge, Y. Zhang, Y.-J. Heo, and S.-J. Park, "Advanced Design and Synthesis of Composite Photocatalysts for the Remediation of Wastewater: A Review," *Catalysts*, vol. 9, no. 2, p. 122, Jan. 2019, doi: 10.3390/catal9020122. <https://doi.org/10.3390/catal9020122>
  25. D. Moitra et al., "Synthesis of a Ni 0.8 Zn 0.2 Fe 2 O 4 -RGO nanocomposite: an excellent a magnetically separable catalyst for dye degradation and microwave absorber," *RSC Adv.*, vol. 6, no. 17, pp. 14090-14096, 2016, doi:10.1039/C5RA26634C. <https://doi.org/10.1039/C5RA26634C>
  26. A. Shokri and S. Karimi, "Treatment of Aqueous Solution Containing Acid red 14 using an Electro Peroxone Process and a Box-Behnken Experimental Design," *Arch. Hyg. Sci.*, vol. 9, no. 1, pp. 48-57, Mar. 2020, doi: 10.29252/ArchHygSci.9.1.48. <https://doi.org/10.29252/ArchHygSci.9.1.48>
  27. S. Chahal, S. Singh, A. Kumar, and P. Kumar, "Oxygen-deficient lanthanum doped cerium oxide nanoparticles for potential applications in spintronics and photocatalysis," *Vacuum*, vol. 177, p. 109395, 2020. <https://doi.org/10.1016/j.vacuum.2020.109395>
  28. S. Chahal, N. Rani, A. Kumar, and P. Kumar, "Electronic structure and photocatalytic activity of samarium doped cerium oxide nanoparticles for hazardous rose bengal dye degradation," *Vacuum*, vol. 172, p. 109075, 2020. <https://doi.org/10.1016/j.vacuum.2019.109075>
  29. D. H. K. Reddy and Y.-S. Yun, "Spinel ferrite magnetic adsorbents: Alternative future materials for water purification?," *Coord. Chem. Rev.*, vol. 315, pp. 90-111, May 2016, doi: 10.1016/j.ccr.2016.01.012. <https://doi.org/10.1016/j.ccr.2016.01.012>
  30. L. George, C. Viji, M. Maheen, and E. M. Mohammed, "Synthesis, characterization of Mg/Mn substituted Ni-Zn ferrites and mechanism of their visible light photocatalysis of Methylene Blue and Rhodamine B dyes under magnetic influence," *Mater. Res. Express*, vol. 7, no. 1, p. 015014, Jan. 2020, doi: 10.1088/2053-1591/ab5d26. <https://doi.org/10.1088/2053-1591/ab5d26>
  31. J.-M. Herrmann, "Photocatalysis fundamentals revisited to avoid several misconceptions," *Appl. Catal. B Environ.*, vol. 99, no. 3-4, pp. 461-468, Sep. 2010, doi: 10.1016/j.apcatb.2010.05.012. <https://doi.org/10.1016/j.apcatb.2010.05.012>
  32. R. Saravanan, F. Gracia, and A. Stephen, "Basic Principles, Mechanism, and Challenges of Photocatalysis," in *Nanocomposites for Visible Light-induced Photocatalysis*, M. M. Khan, D. Pradhan, and Y. Sohn, Eds. Cham: Springer International Publishing, 2017, pp. 19-40. doi: 10.1007/978-3-319-62446-4\_2. [https://doi.org/10.1007/978-3-319-62446-4\\_2](https://doi.org/10.1007/978-3-319-62446-4_2)
  33. Y. Zeng et al., "Fabrication of Z-scheme magnetic  $\text{MoS}_2/\text{CoFe}_2\text{O}_4$  nanocomposites with highly efficient photocatalytic activity," *J. Colloid Interface Sci.*, vol. 514, pp. 664-674, Mar. 2018, doi: 10.1016/j.jcis.2017.12.079. <https://doi.org/10.1016/j.jcis.2017.12.079>
  34. R. Shu et al., "Fabrication of 3D net-like MWCNTs/ $\text{ZnFe}_2\text{O}_4$  hybrid composites as high-performance electromagnetic wave absorbers," *Chem. Eng. J.*, vol. 337, pp. 242-255, Apr. 2018, doi: 10.1016/j.cej.2017.12.106. <https://doi.org/10.1016/j.cej.2017.12.106>
  35. B. D. Cullity, *Elements of X-ray diffraction*. Reading, Mass.: Addison-Wesley Pub. Co., 1956.
  36. H. M. Abdelmoneim, "Optical properties of  $\text{Ti}_0.5\text{Li}_0.5\text{La}_0.1\text{Fe}_1.9\text{O}_4$  ferrite thin film," *Phys. B Condens. Matter*, vol. 405, no. 6, pp. 1551-1557, Mar. 2010, doi: 10.1016/j.physb.2009.12.038. <https://doi.org/10.1016/j.physb.2009.12.038>
  37. J. Tauc, Ed., *Amorphous and Liquid Semiconductors*. Boston, MA: Springer US, 1974. doi: 10.1007/978-1-4615-8705-7. <https://doi.org/10.1007/978-1-4615-8705-7>
  38. J. Liqiang et al., "Review of photoluminescence performance of nano-sized semiconductor materials and its relationships with photocatalytic activity," *Sol. Energy Mater. Sol. Cells*, vol. 90, no. 12, pp. 1773-1787, Jul. 2006, doi: 10.1016/j.solmat.2005.11.007. <https://doi.org/10.1016/j.solmat.2005.11.007>
  39. X. Z. Li, F. B. Li, C. L. Yang, and W. K. Ge, "Photocatalytic activity of  $\text{WO}_x\text{-TiO}_2$  under visible light irradiation," *J. Photochem. Photobiol. Chem.*, vol. 141, no. 2, pp. 209-217, Jul. 2001, doi: 10.1016/S1010-6030(01)00446-4. [https://doi.org/10.1016/S1010-6030\(01\)00446-4](https://doi.org/10.1016/S1010-6030(01)00446-4)
  40. R. D. Waldron, "Infrared Spectra of Ferrites," *Phys. Rev.*, vol. 99, no. 6, pp. 1727-1735, Sep. 1955, doi: 10.1103/PhysRev.99.1727. <https://doi.org/10.1103/PhysRev.99.1727>
  41. K. N. Harish, H. S. Bhojya Naik, P. N. Prashanth Kumar, and R. Viswanath, "Synthesis, enhanced optical and photocatalytic study of Cd-Zn ferrites under sunlight," *Catal. Sci. Technol.*, vol. 2, no. 5, p. 1033, 2012, doi: 10.1039/c2cy00503d. <https://doi.org/10.1039/c2cy00503d>
  42. S. Xu, W. Shanguan, J. Yuan, J. Shi, and M. Chen, "Photocatalytic Properties of Bismuth Titanate  $\text{Bi}_2\text{TiO}_7$  Prepared by Co-Precipitation Processing," *Mater. Sci. Eng. B*, vol. 137, pp. 108-111, Feb. 2007, doi: 10.1016/j.mseb.2006.10.019. <https://doi.org/10.1016/j.mseb.2006.10.019>
  43. S. E. Shirath, "STRUCTURAL PROPERTIES AND CATION DISTRIBUTION OF Co-Zn NANOFERRITES," *Int. J. Mod. Phys. B*, Jan. 2009, Accessed: Feb. 24, 2023. [Online]. Available: [https://www.academia.edu/3434769/STRUCTURAL\\_PROPERTIES\\_AND\\_CATION\\_DISTRIBUTION\\_OF\\_Co\\_Zn\\_NANOFERRITES](https://www.academia.edu/3434769/STRUCTURAL_PROPERTIES_AND_CATION_DISTRIBUTION_OF_Co_Zn_NANOFERRITES)
  44. B. S. Holinsworth et al., "Chemical tuning of the optical band gap in spinel ferrites:  $\text{CoFe}_2\text{O}_4$  vs  $\text{NiFe}_2\text{O}_4$ ," *Appl. Phys. Lett.*, vol. 103, no. 8, p. 082406, Aug. 2013, doi: 10.1063/1.4818315. <https://doi.org/10.1063/1.4818315>
  45. J.-G. Yu, H.-G. Yu, B. Cheng, X.-J. Zhao, J. C. Yu, and W.-K. Ho, "The Effect of Calcination Temperature on the Surface Microstructure and Photocatalytic Activity of  $\text{TiO}_2$  Thin Films Prepared by Liquid Phase Deposition," *J. Phys. Chem. B*, vol. 107, no. 50, pp. 13871-13879, Dec. 2003, doi: 10.1021/jp036158y. <https://doi.org/10.1021/jp036158y>
  46. K. L. Routray, S. Saha, and D. Behera, "Effect of CNTs blending on the structural, dielectric and magnetic properties of nanosized cobalt ferrite," *Mater. Sci. Eng. B*, vol. 226, pp. 199-205, Dec. 2017, doi: 10.1016/j.mseb.2017.09.021. <https://doi.org/10.1016/j.mseb.2017.09.021>



47. "Polyaniline-Coated  $\text{Fe}_3\text{O}_4$  Nanoparticle-Carbon-Nanotube Composite and its Application in Electrochemical Biosensing - Liu - 2008 - Wiley Online Library." <https://onlinelibrary.wiley.com/doi/abs/10.1002/sml.200701018> (accessed Feb. 25, 2023). <https://doi.org/10.1002/sml.200701018>
48. K. K. Kefeni and B. B. Mamba, "Photocatalytic application of spinel ferrite nanoparticles and nanocomposites in wastewater treatment: Review," *Sustain. Mater. Technol.*, vol. 23, p. e00140, Apr. 2020, doi: 10.1016/j.susmat.2019.e00140. <https://doi.org/10.1016/j.susmat.2019.e00140>
49. F. Aisien, A. Amenaghawon, and E. Ekpenisi, "Photocatalytic decolourisation of industrial wastewater from a soft drink company," *J. Eng. Appl. Sci.*, vol. 9, pp. 11-16, Apr. 2014.
50. A. Šutka et al., "Ag sensitized  $\text{TiO}_2$  and  $\text{NiFe}_2\text{O}_4$  three-component nanoheterostructures: synthesis, electronic structure and strongly enhanced visible light photocatalytic activity," *RSC Adv.*, vol. 6, no. 23, pp. 18834-18842, Feb. 2016, doi: 10.1039/C6RA00728G. <https://doi.org/10.1039/C6RA00728G>
51. T. Harifi and M. Montazer, "A novel magnetic reusable nanocomposite with enhanced photocatalytic activities for dye degradation," *Sep. Purif. Technol.*, vol. 134, pp. 210-219, Sep. 2014, doi: 10.1016/j.seppur.2014.06.042. <https://doi.org/10.1016/j.seppur.2014.06.042>
52. W. Jiang, X. Zhang, X. Gong, F. Yan, and Z. Zhang, "Sonochemical synthesis and characterization of magnetic separable  $\text{Fe}_3\text{O}_4$ - $\text{TiO}_2$  nanocomposites and their catalytic properties," *Int. J. Smart Nano Mater.*, vol. 1, no. 4, pp. 278-287, Nov. 2010, doi: 10.1080/19475411.2010.528873. <https://doi.org/10.1080/19475411.2010.528873>
53. L. T. T. Nguyen et al., "A Facile Synthesis, Characterization, and Photocatalytic Activity of Magnesium Ferrite Nanoparticles via the Solution Combustion Method," *J. Chem.*, vol. 2019, pp. 1-8, Mar. 2019, doi: 10.1155/2019/3428681. <https://doi.org/10.1155/2019/3428681>
54. J. Low, J. Yu, M. Jaroniec, S. Wageh, and A. A. Al-Ghamdi, "Heterojunction Photocatalysts," *Adv. Mater.*, vol. 29, no. 20, p. 1601694, May 2017, doi: 10.1002/adma.201601694. <https://doi.org/10.1002/adma.201601694>